method [13], the beads possess a wide size distribution with a standard deviation of 70 μm. Preparation of smaller beads of less than 300 μm with a narrow size distribution has been impractical to date, due particularly to nozzle diameter limitations, the narrowest being a 250 μm outer diameter for a 31 gauge needle. Furthermore, productivity decreases drastically when thinner needles are used because of the high-pressure loss.

The application of micromachining techniques has increased rapidly in biotechnology in the last decade [14,15]. We recently proposed a novel device for preparing monodispersed emulsion droplets from 3 to 100 μm using a microfabricated channel array [16–18]. We demonstrate in this study a novel microfluidics device that utilizes a silicon micro-nozzle (MN) array, enabling to prepare 50–200 μm calcium alginate beads. Sodium alginate aqueous solution was extruded into the laminar flow of soybean oil through an MN, and size-controlled alginate droplets were formed. Alginate droplets were immediately reacted with $CaCl_2$ droplets to form calcium alginate beads.

2. Materials and methods

2.1. Experimental setup for alginate beads formation

The laboratory-scale apparatus for beads formation, which is depicted in Fig. 1, was similar to the apparatus for emulsion formation [19]. The MNs were fabricated by photolithography and the two-step deep reactive ion-etching process [19]. The MN has an inner width of 30 μm, an outer width of 60 μm, and a nozzle height of 15 μm. The flow channels inside the MNs are fabricated through a 500-μm-thick silicon plate.

2.2. Alginate beads formation

Sodium alginate (IL-2) was kindly provided from Kimica Corp. (Tokyo, Japan) and dissolved in HEPES buffered saline at the concentration of 1.5%. Soybean oil was purchased from Wako Pure Chemical, Ind. (Osaka, Japan). Alginate solution was fed into the flow of soybean oil through the MN in the upper stream of the soybean oil flow, and $CaCl_2$ 0.1 M aqueous solution containing 0.14 M NaCl was fed through MN in the downstream area of the oil flow as shown in Fig. 1c. The formed alginate droplets and $CaCl_2$ droplets collide with each other in the stream of soybean oil, and the reaction between the alginate and Ca^{2+} proceeds by coalescence of the droplets. No surfactant was added in the system to promote coalescence.

For encapsulating living cells, a 1.5% sodium alginate solution containing cells at 1×10^7 cells/ml

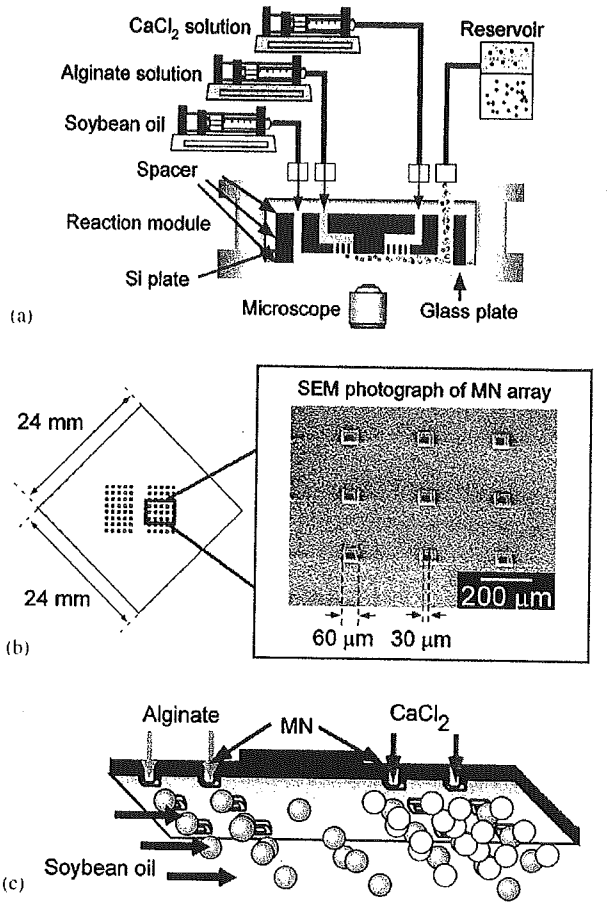

Fig. 1. Equipment for the alginate beads formation system and schematics of the beads preparation process. (a) Schematics of the experimental equipment. (b) Schematics of the silicon plate and SEM photograph of the MN array fabricated on a silicon plate. (c) Schematic flows in the reaction module.

was extruded through the MNs into the oil flow to prepare alginate beads. The calcium alginate beads were formed as described above, and treated with lipase solution containing 0.1% lipase (Amano PS, Amano Enzyme Inc., Aichi, Japan) at 37 °C for 10 min, and washed with washing buffers ($CaCl_2$ solution and HBS).

2.3. Cell culture

Human kidney 293 cells were obtained from the Japan health science foundation (Tokyo, Japan) and transfected with pIRES2-EGFP vector (Clontech Laboratories, Inc., Palo Alto, CA, USA) encoding GFP using an adenovirus. The transfected cells (293/GFP) were cultured in Dulbecco's modified Eagle medium (DMEM; Sigma-Aldrich Co., St. Louis, MO, USA) supplemented with 10% heat-inactivated fetal bovine serum (Sigma-Aldrich Co.).

2.4. Measurement and analytical method

Scanning electron microscopy photographs were taken with a JSM-5600LC (JEOL Ltd., Tokyo, Japan). The number-average diameters (D [μm]) and coefficients of variation (CV [%]; percentage of standard deviation) of the droplets/beads were determined from pictures of 100 droplets/beads. Average values of roundness (R) were used to evaluate the shape of the prepared beads, which is defined as

$$R = \frac{4\pi S}{L^2}, \quad (1)$$

where S is the projection area of beads and L is the perimeter of the beads. Winroof (Mitani Corporation, Fukui, Japan) software was used to analyze the captured images.

3. Results

3.1. Droplet formation process from MN

Sodium alginate aqueous solution was extruded into the flow of soybean oil through an MN. The oil flow rates were 200 and 1000 ml/h, corresponding to flow velocities of 26 and 128 mm/s. The flow rate of the alginate solution was identical in both series. That is 5 ml/h, corresponding to flow velocities of 15 mm/s in each nozzle. One hundred and four nozzles produce alginate droplets in the present system. The alginate solution fed from the MN was sheared by the flow of soybean oil and monodispersed droplets were formed as shown in Figs. 2a and b. Smaller droplets were formed in a faster flow velocity of the soybean oil because of the higher viscous drag force. The number-average diameters and CVs of the droplets were 247 μm and 5.0% for 26 mm/s flow velocity and 88.4 μm and 5.9% for 128 mm/s flow velocity. The Reynold's numbers in these experimental conditions were 0.25 and 1.23, which means oil flow was laminar flow.

3.2. Beads formation process

The prepared alginate droplets were required to react with $CaCl_2$ solution for gel formation. $CaCl_2$ aqueous solution was extruded through the MN at the downstream area of the oil flow at the flow rate of 100 ml/h, which is 20 times greater than that of the alginate solution. The excess amount of $CaCl_2$ solution compared to alginate solution is expected to prevent coalescence between the alginate droplet and alginate droplet. Calcium alginate beads were formed by reaction between the alginate droplets and $CaCl_2$ droplets. Most of the prepared beads had spherical or ellipsoidal shapes as shown in Figs. 2c and d. The values of roundness of the prepared beads were 0.95 for 26 mm/s of oil flow and 0.97 for 128 mm/s of oil flow. Figs. 2e and f illustrate the changes in diameter distribution between the liquid droplets before gelation and gel beads after gelation. The number-average diameters and CVs of the prepared beads were 216 μm and 14.4% for 26 mm/s of oil flow and 77.4 μm and 11.1% for 128 mm/s of oil flow. The droplet's diameter had decreased by 13% from their original droplet diameter after bead formation in each case. Secondary peaks were observed at values 1.25 times greater than the mean values, which correspond to twice as much volume (Figs. 2e and f). Some of the alginate droplets may coalesce with each other before coalescence with the $CaCl_2$ solution. The coefficients of variation of the prepared beads were slightly increased,

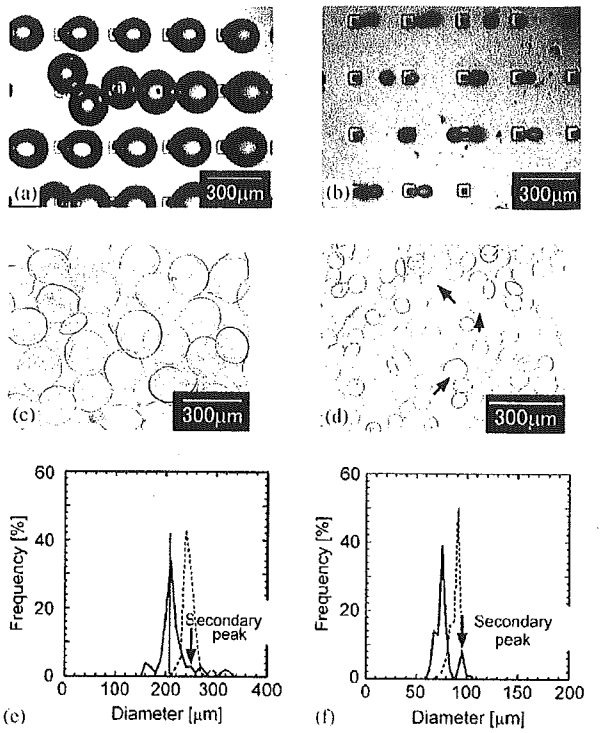

Fig. 2. Droplet formation process and prepared calcium alginate beads at different flow velocities of soybean oil. Microscope photographs of the alginate droplet formation process for: (a) 26 mm/s flow velocities of soybean oil during droplet formation process and (b) 128 mm/s flow velocities of soybean oil. Microscope photographs of prepared alginate beads for: (c) 26 mm/s flow velocities of soybean oil during droplet formation process and (d) 128 mm/s flow velocities of soybean oil during droplet formation process. The beads 1.25 times larger than the mean values (two times larger in volume) were observed (arrows in (d)). Diameter distribution of droplets and beads for: (e) 26 mm/s flow velocities of soybean oil and (f) 128 mm/s flow velocities of soybean oil. The liquid droplet diameter distributions are indicated by the dotted line, and the gel-bead diameter distributions are indicated by the solid line. The secondary peaks 1.25 times larger than the mean values (two times larger in volume) were observed (arrows in (e, f)).

but the prepared beads maintained a narrow diameter distribution after bead formation.

The bead formation system proposed in this study can be applied for encapsulation of living cells, since the system works under sterile conditions. Human fetal kidney 293/GFP cells were entrapped in the calcium–alginate beads using the MN system. The flow velocity of the oil was 103 mm/s. The flow rate of the alginate solution was 10 ml/h, and the flow rate of the $CaCl_2$ solution was 100 ml/h. Cell-containing calcium alginate beads were successfully prepared using MN system as depicted in Fig. 3. The prepared alginate beads were easily dispersed in the aqueous solution after lipase treatment. The number-average diameters and coefficients of variation of the prepared droplets and beads were 169 μm and 8.0% for droplets and 162 μm and 28% for beads. Several beads appeared fragmented in Fig. 3. In our observation, 11% of the prepared beads had neither spherical nor ellipsoidal shape, which had been fragmented or deformed. Green fluorescence from the GFP produced by the cells entrapped in the alginate beads is depicted in Fig. 3b, indicating that living cells were successfully encapsulated in the calcium alginate beads.

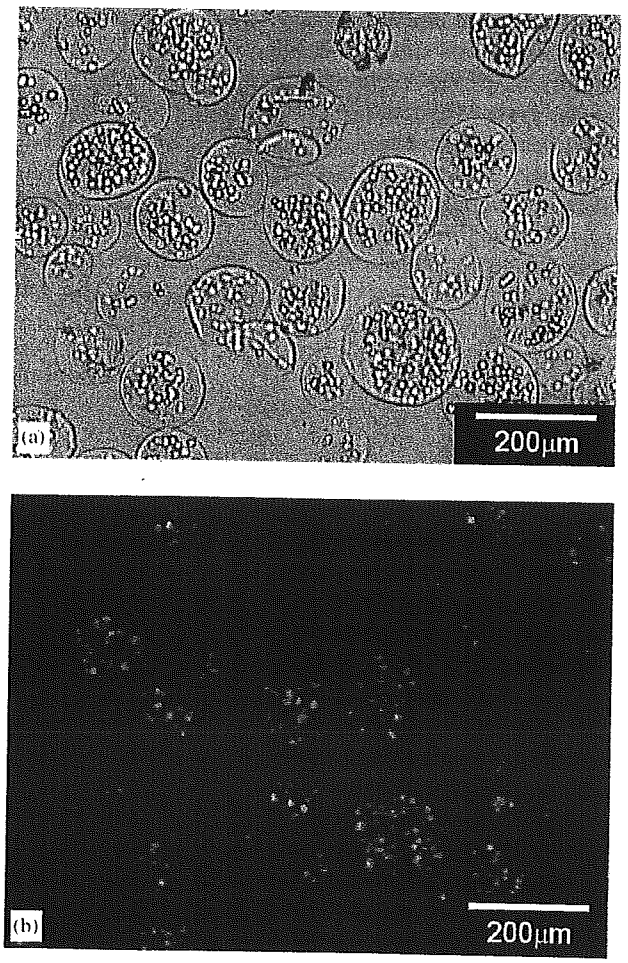

Fig. 3. Cell encapsulation into calcium alginate beads. Microscope photographs of calcium alginate beads containing 293/GFP cells observed in a bright field (a) and fluorescence mode (b).

4. Discussion

The MN described here has a thinner and shorter structure than commercially available needles (typically with an outer diameter of 250 μm and needle length of 12.7 mm for 31 gauge and 1/2 in needle), which is advantageous in terms of preciseness and low-pressure loss. The device utilizes the features of microfluidics (i.e. significant viscous force and laminar flow) and it leads to stable shearing during droplet formation. The droplet–droplet reaction system demonstrated in this study has the advantages of a large surface area of reaction liquid, which creates an opportunity for an immediate reaction between the alginate droplet and $CaCl_2$ solution. The above advantages enable the beads prepared in this study to be smaller and have a narrower diameter distribution compared to conventional methods.

The productivity of alginate beads was determined by the flow rate of the alginate solution. Stable droplet formation was possible in the present system up to an alginate flow rate of 20 ml/h using one hundred and four nozzles. The productivity of alginate droplets from the unit silicon plate area was 214 ml/(cm^2 h). The low-pressure loss structure of the device leads to high productivity as an air-flow method and electrostatic droplet generation method despite the present small-scale apparatus. Though the productivity with the vibrating nozzle method (i.e. 600 ml/h) [20] is higher than the present system, it may decrease for preparing beads smaller than 300 μm because of the high-pressure loss caused by the thin needle. The scale-up of productivity to 1000 times would be possible by utilizing a large silicon plate and an accumulation of multiple silicon plates. Therefore, we believe that the productivity of the present system is sufficiently high for us to overcome the limitation of productivity by scale-up.

The nozzle-type exit shape is beneficial especially in producing alginate beads containing biological cells. It prevents wetting of the silicon plate surface with the dispersed aqueous phase. This leads to better droplet detachment, which is important for continuous shearing and stable droplet formation. The beads were formed under sterile conditions and without chemically irritant materials such as surfactant, which enabled successful encapsulation of living cells in the alginate beads. The viability of the entrapped cells in Fig. 3 is roughly estimated as 70%. The CV for beads containing cells increased. Inhomogeneous structure of the cell containing alginate solution affected the droplet formation

process and led to the formation of a different sized droplet. Substances secreted from the cells would disturb the coalescence between alginate droplets and $CaCl_2$ droplets. The alginate beads of 50–200 μm with a narrow size distribution are useful carriers for cell immobilization since they provide better transportation of nutrients and oxygen. The beads prepared by this method would be useful as sophisticated biomaterials; for example, as cell transplantation carriers, drug carriers, and scaffold for tissue engineering and cell cultures because of their characteristic physical, chemical, and biological properties.

5. Conclusions

We presented here a novel microfabricated device enabling to prepare size-controlled small calcium alginate beads less than 300 μm. The unique characteristics of our device include (a) a thin (30 μm × 30 μm) and short (500 μm) silicon nozzle, (b) droplet formation by viscous drag force of the oil flow, (c) a droplet–droplet reaction for gel formation, and (d) a nozzle-type exit shape (but not a flat exit pore). Using this device, the alginate beads with diameters of 50–200 μm and coefficients of variation of less than 15% were successfully prepared. The living cells were successfully encapsulated into 162 μm calcium alginate beads with maintaining viability. The smaller alginate beads of 50–200 μm prepared by this device are expected to be used in various fields, including medical, pharmaceutical, and bioengineering fields.

Acknowledgments

We thank Dr. T. Maruyama (Kyushu University) for useful information about lipase. We thank Mr. Y. Sando (Konica Minolta Holdings, Inc.) for helping with fabrication of the silicon plate. This work was supported by the Nanotechnology Project, Ministry of Agriculture, Forestry and Fisheries, and the Program for Promotion of Fundamental Studies in Health Sciences of the Organization for Pharmaceutical Safety and Research of Japan.

References

[1] Lim F, Sun AM. Microencapsulated islets as bioartificial endocrine pancreas. Science 1980;210:908–10.
[2] De Vos P, Van Hoogmoed CG, Van Zanten J, Netter S, Strubbe JH, Busscher HJ. Long-term biocompatibility, chemistry, and function of microencapsulated pancreatic islets. Biomaterials 2003;24:305–12.
[3] AlHendy A, Hortelano G, Tannenbaum GS, Chang PL. Growth retardation—an unexpected outcome from growth hormone gene therapy in normal mice with microencapsulated myoblasts. Hum Gene Ther 1996;7:61–70.
[4] Read TA, Sorensen DR, Mahesparan R, Enger PØ, Timpl R, Olsen BR, Hjelstuen MHB, Haraldseth O, Bjerkvig R. Local endostatin treatment of gliomas administered by microencapsulated producer cells. Nat Biotechnol 2001;19:29–34.
[5] Joki T, Machluf M, Atala A, Zhu JH, Seyfried NT, Dunn IF, Abe T, Carroll RS, Black PM. Continuous release of endostatin from microencapsulated engineered cells for tumor therapy. Nat Biotechnol 2001;19:35–9.
[6] Cirone P, Bourgeois JM, Chang PL. Antiangiogenic cancer therapy with microencapsulated cells. Hum Gene Ther 2003;14:1065–77.
[7] Kwon YJ, Peng CA. Calcium-alginate gel bead cross-linked with gelatin as microcarrier for anchorage-dependent cell culture. Biotechniques 2002;33:212–8.
[8] Wang L, Shelton RM, Cooper PR, Lawson M, Triffitt JT, Barralet JE. Evaluation of sodium alginate for bone marrow cell tissue engineering. Biomaterials 2003;24:3475–81.
[9] Stevens MM, Qanadilo HF, Langer R, Shastri VP. A rapid-curing alginate gel system: utility in periosteum-derived cartilage tissue engineering. Biomaterials 2004;25:887–94.
[10] Chicheportiche D, Reach G. In vitro kinetics of insulin release by microencapsulated rat islets: effect of the size of the microcapsules. Diabetologia 1988;31:54–7.
[11] Leblond FA, Simard G, Henley N, Rocheleau B, Huet PM, Halle JP. Studies on smaller (−315 μM) microcapsules: IV. Feasibility and safety of intrahepatic implantations of small alginate poly-L-lysine microcapsules. Cell Transplant 1999;8:327–37.
[12] Dulieu C, Poncelet D, Neufeld RJ. Encapsulation and immobilization techniques. In: Kühtreiber WM, Lanza RP, Chick WL, editors. Cell encapsulation technology and therapeutics. Boston: Birkhäuser; 1999. p. 3–17.
[13] Bugarski B, Li Q, Goosen MFA, Poncelet D, Neufeld RJ, Vunjak G. Electrostatic droplet generation: mechanism of polymer droplet formation. AIChE J 1994;40:1026–31.
[14] Hong JW, Studer V, Hang G, Anderson WF, Quake SR. A nanoliter-scale nucleic acid processor with parallel architecture. Nat Biotechnol 2004;22:435–9.
[15] Meldrum DR, Holl MR. Microscale bioanalytical systems. Science 2002;297:1197–8.
[16] Sugiura S, Nakajima M, Iwamoto S, Seki M. Interfacial tension driven monodipersed droplet formation from microfabricated channel array. Langmuir 2001;17:5562–6.
[17] Kawakatsu T, Kikuchi Y, Nakajima M. Regular-sized cell creation in microchannel emulsification by vidual microprocessing method. J Am Oil Chem Soc 1997;74:317–21.
[18] Sugiura S, Nakajima M, Kumazawa N, Iwamoto S, Seki M. Characterization of spontaneous transformation-based droplet formation during microchannel emulsification. J Phys Chem B 2002;106:9405–9.
[19] Kobayashi I, Nakajima M, Chun K, Kikuchi Y, Fujita H. Silicon array of elongated through-holes for monodisperse emulsion droplets. AIChE J 2002;48:1639–44.
[20] Brandenberger HR, Widmer F. Immobilization of highly concentrated cell suspensions using the laminar jet breakup technique. Biotechnol Progr 1999;15:366–72.

Original Report

Ukihide Tateishi[1]
Tadashi Hasegawa[2]
Hiroaki Onaya[1]
Mitsuo Satake[1]
Yasuaki Arai[1]
Noriyuki Moriyama[1]

Myxoinflammatory Fibroblastic Sarcoma: MR Appearance and Pathologic Correlation

OBJECTIVE. The purpose of our study was to define the MR appearance of myxoinflammatory fibroblastic sarcoma of the soft tissues and to make correlations with the histopathologic features.

CONCLUSION. Myxoinflammatory fibroblastic sarcoma is an uncommon malignancy that typically affects adult subjects, who present with painless swelling. This lesion manifests on MR images as a poorly circumscribed mass involving the underlying tendon sheath in the distal extremities.

Myxoinflammatory fibroblastic sarcoma of the soft tissues is a rare low-grade tumor of uncertain origin that usually arises in the hands and feet. Myxoinflammatory fibroblastic sarcoma was first described in 1998 by Meis-Kindblom and Kindblom [1]. Montgomery et al. [2] named the tumor "inflammatory myxohyaline tumor" of the distal extremities with virocyte or Reed-Sternberg-like cells. Histologic characteristics are the spindle to epithelioid neoplastic cells as the manifestation of malignancy admixed with the myxoid and hyalinized matrix, the inflammatory infiltrate, and bizarre virocyte or Reed-Sternberg-like cells with enlarged vesicular nuclei [1–3].

More than 100 cases of myxoinflammatory fibroblastic sarcoma have been reported, with a large series identified in two articles [1–6]. However, MRI findings of myxoinflammatory fibroblastic sarcoma have rarely been documented. The purpose of this study was to characterize the MR appearance of myxoinflammatory fibroblastic sarcoma and to correlate that appearance with the histopathologic features.

Materials and Methods

MR images of all patients with pathologically proven myxoinflammatory fibroblastic sarcoma at our institution were retrospectively reviewed. Our institutional review board gave its approval for a review of patient records and images. The patients were identified by review of our institution's pathology database for a 2-year period. The affected patients included three males and one female who ranged in age from 15 to 62 years old (mean age, 35 years). All histopathologic specimens were reviewed by an experienced pathologist to confirm the diagnosis. Histopathologic examination in all patients showed spindle and epithelioid tumor cells with mild nuclear atypia. Ganglionlike cells and Reed-Sternberg-like cells were also prominent in all cases. Inflammatory cells, including neutrophils, lymphocytes, and eosinophils, were densely present in all cases. Immunohistochemistry was performed in all patients, and all tumors displayed immunoreactivity to vimentin, smooth-muscle actin, and CD34. These histopathologic characteristics were compatible with the diagnosis of myxoinflammatory fibroblastic sarcoma [7]. Medical records were reviewed by one of the authors for presenting complaints, disease progression, and outcome. Radiographs, available for all patients, were also evaluated by two radiologists for the presence of soft-tissue masses or nodules, mineralization, and bone destruction. The findings were recorded by consensus.

T1- and T2-weighted MR images were obtained in the sagittal and coronal planes using a surface coil. T1-weighted conventional spin-echo MR images were obtained using a 20-cm field of view, 3.5- to 5-mm section thickness, TR range/TE of 450–520/15, 160 × 256 matrix, and 2 signals acquired. T2-weighted fast spin-echo acquisitions with ($n = 3$) or without ($n = 1$) fat suppression were performed using a 20-cm field of view, 3.5- to 5-mm section thickness, 3,600–4,000/120, 160 × 256 ma-

Received June 2, 2004; accepted after revision July 28, 2004.

Supported in part by grant for Scientific Research Expenses for Health and Welfare Programs, The Foundation for the Promotion of Cancer Research, and second-term Comprehensive 10-year Strategy for Cancer Control.

[1]Division of Diagnostic Radiology, National Cancer Center Hospital and Institute, Tsukiji, Chuo-Ku, 104-0045, Tokyo, Japan. Address correspondence to U. Tateishi.

[2]Pathology Division, National Cancer Center Hospital and Institute, Tsukiji, Tokyo, Japan.

AJR 2005;184:1749–1753

0361–803X/05/1846–1749

trix, and 2 signals acquired. After the IV administration of 0.1 mmol of gadopentetate dimeglumine (Magnevist, Schering) per kilogram of body weight, transverse T1-weighted images with ($n = 3$) or without ($n = 1$) fat suppression were obtained in the sagittal and coronal planes.

MR images were reviewed by two radiologists and findings were recorded by consensus. Images were evaluated for lesion location and size, depth (superficial or deep), shape of margin (well or ill defined), and the presence or absence of extracompartmental extension. To define depth, superficial lesions did not involve the superficial fascia, and deep lesions were deep in relation to or invaded the superficial fascia. The relationship between tumor and the underlying tendon sheath was also evaluated. MR images were evaluated for predominant signal intensity characteristics (low, intermediate, high), signal homogeneity or heterogeneity, and enhancement characteristics. On T1-weighted images, low signal intensity was defined as signal intensity less than that of muscle; intermediate signal intensity, similar to that of muscle; and high signal intensity, similar to that of fat. On T2-weighted images, low signal intensity was defined as signal intensity similar to that of muscle; intermediate signal intensity, greater than that of muscle but less than that of fat; and high signal intensity, equal to or greater than that of fat. Tumor enhancement was visually graded as greater than, less than, or equal to that of surrounding muscle and vessels.

Results

Clinical Features

All patients were symptomatic at presentation. Presenting complaints were painless swelling of the distal extremities. The mean symptom duration was 4.8 months. Tumors arose from the feet ($n = 2$), hands ($n = 1$), and fingers ($n = 1$). All patients received excisional biopsy for definitive diagnosis and primary therapy. Surgical margins were adequate in three patients and inadequate in one patient. The one patient with an inadequate surgical margin underwent subsequent wide resection. Chemotherapy and radiation therapy were not included in the treatment regimen in any patient. Local recurrence occurred 26.5 months after the initial surgery in two patients. These patients received wide resection. At the latest follow-up (27–82 months; mean, 45 months), no patients had developed further recurrence or metastasis.

MRI Findings and Pathologic Correlations

The gross characteristics of the resected specimens featured multinodular architecture corresponding to MRI features. The mean tumor diameter was 2.4 cm (range, 1.2–3.0 cm). Tumors were located along the tendon sheath in all patients. Findings of extensive involvement surrounding the tendon sheath by the tumor were seen. In two patients, the tumor existed beneath the tendon sheath (Fig. 1), and in two it involved the surrounding tendon sheath diffusely and focally infiltrated the dermis (Fig. 2). One patient had an ill-defined, irregularly marginated mass involving the ulnar nerve and the tendon sheath of the flexor carpi ulnaris (Fig. 2).

Cortical invasion was not identified in any patient on radiographs. All tumors showed predominantly low signal intensity relative to muscle on T1-weighted MR images (Fig. 3). Two lesions showed moderate and homogeneous enhancement after the IV administration of contrast material (Figs. 1 and 3). The cut surface of resected specimens showed solid nests of neoplastic cells that featured spindle and epithelioid cells with higher cellularity, which corresponded to homogeneous enhancement on contrast-enhanced MR images. Two lesions showed heterogeneous enhancement of the tumor that correlated with geographic areas of the myxoid stromal matrix on microscopic observations (Fig. 4). On T2-weighted MR images, all lesions had intermediate signal intensity greater than that of muscle but less than that of fat (Fig. 2). In all cases, the cut surface of specimens revealed solid nests of cellular areas with foci of hyalinized collagen fibers and hypocellular areas with a myxoid stromal

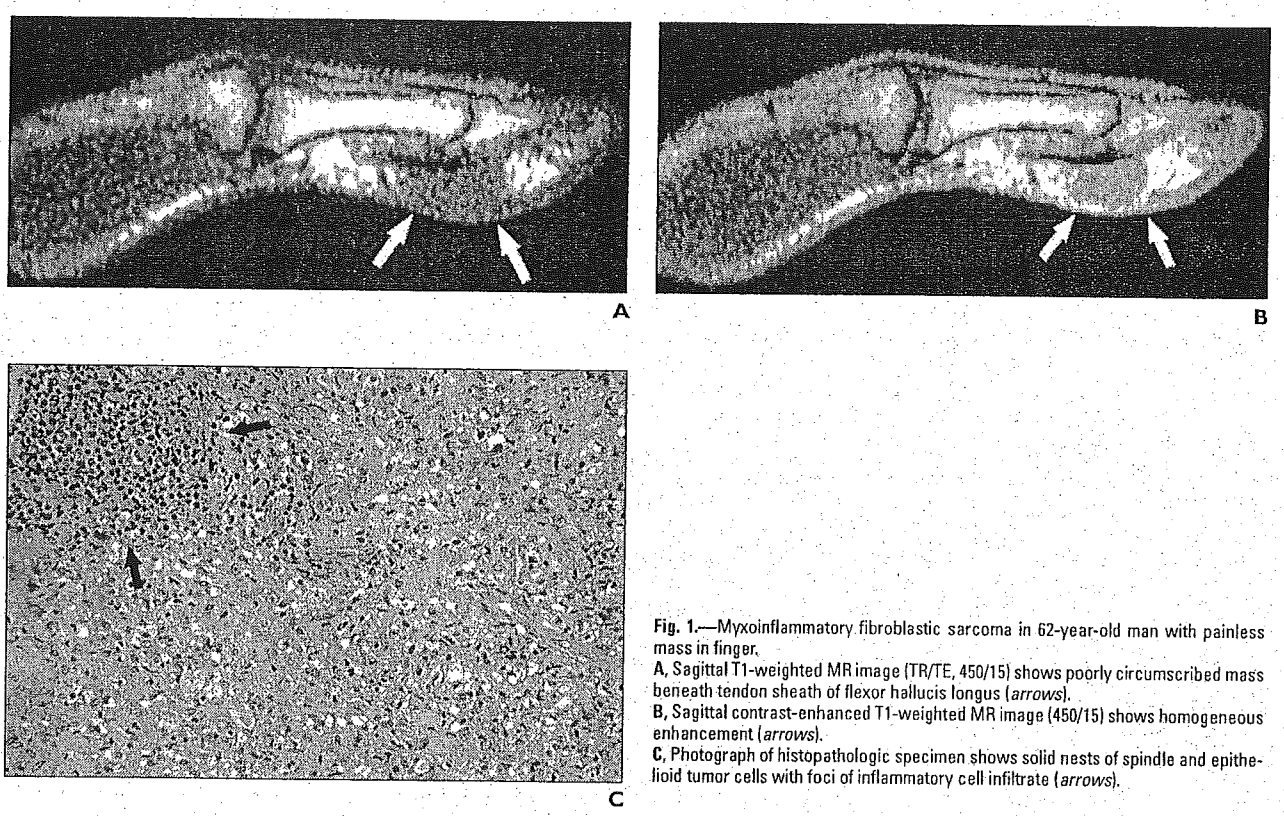

Fig. 1.—Myxoinflammatory fibroblastic sarcoma in 62-year-old man with painless mass in finger.
A, Sagittal T1-weighted MR image (TR/TE, 450/15) shows poorly circumscribed mass beneath tendon sheath of flexor hallucis longus (*arrows*).
B, Sagittal contrast-enhanced T1-weighted MR image (450/15) shows homogeneous enhancement (*arrows*).
C, Photograph of histopathologic specimen shows solid nests of spindle and epithelioid tumor cells with foci of inflammatory cell infiltrate (*arrows*).

matrix, which corresponded to the imaging appearance of intermediate signal intensity on T2-weighted MR images.

Two patients developed recurrent tumors and underwent follow-up MRI after treatment. One patient developed a mass of sheetlike appearance beneath the dorsal portion of the underlying tendon sheath (Fig. 3). Signal characteristics and homogeneous enhancement patterns were similar to those of the primary tumors. Histopathologic examination of this patient showed an infiltrate of lymphoid cells and a marked proliferation of spindle-shaped tumor cells surrounding the tendon sheaths.

In the second patient, a mass of branching pattern occurred along the extensor digitorum longus tendon sheaths of the second and fourth toes without distortion of the architecture of the tendon sheaths (Fig. 4). This patient had also MRI findings suggesting capsular involvement in the metatarsophalangeal joint of the second toe. Histopathologic examination revealed that the tumor arose from the extensor digitorum longus tendon sheaths and also involved the extensor digitorum brevis tendon sheath, cutaneous nerve, and dermis.

Discussion

Myxoinflammatory fibroblastic sarcoma is a rare tumor of the subcutaneous soft tissue that can arise on the trunk but most commonly occurs in the distant extremities [1, 2]. According to the literature and our experience, myxoinflammatory fibroblastic sarcoma is a tumor that most commonly affects adults who are symptomatic at presentation [1, 2]. All patients in our series were symptomatic, with common complaints of a painless mass.

Myxoinflammatory fibroblastic sarcoma has a relatively good prognosis with a long life expectancy despite frequent local recurrence [1–3]. Two of our patients developed local recurrence, with an average duration of 26.5 months. According to the literature, the local recurrence rate in patients with myxoinflammatory fibroblastic sarcoma ranges from 22% to 67% [1, 2]. The metastasis rate in patients with myxoinflammatory fibroblastic sarcoma is uncertain. Metastases have been reported to develop in only a few cases [1].

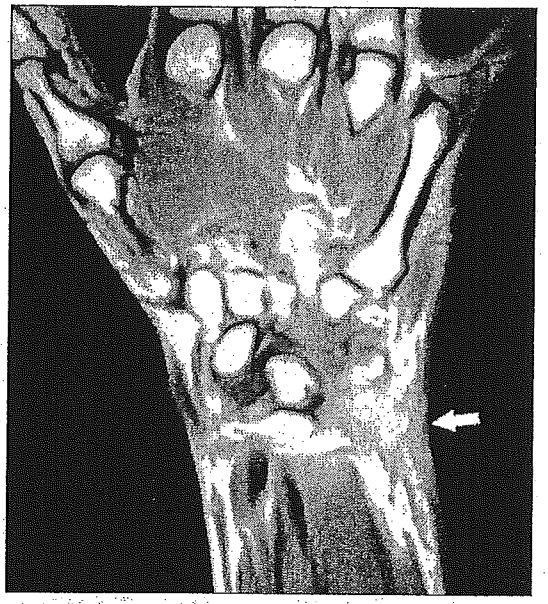

A

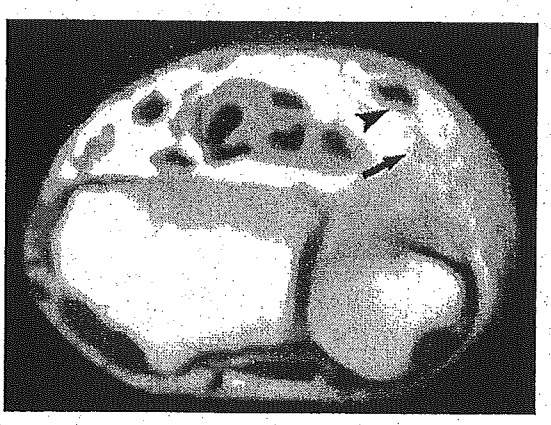

B

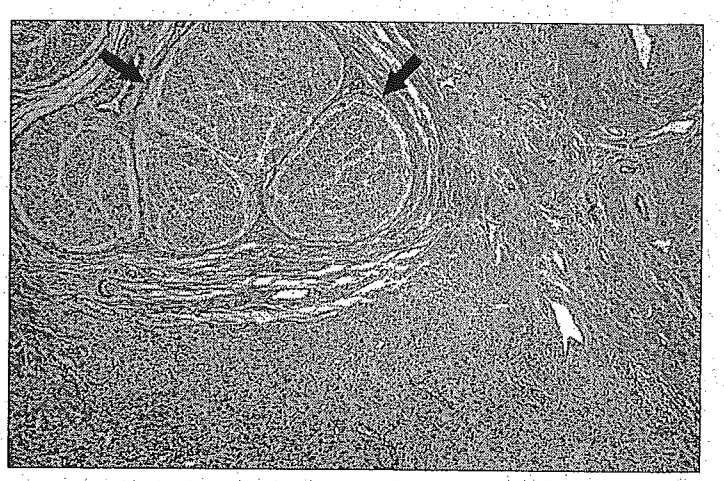

C

Fig. 2.—Myxoinflammatory fibroblastic sarcoma in 31-year-old man with painless mass in subcutaneous soft tissue of wrist.
A, Coronal contrast-enhanced T1-weighted MR image (TR/TE, 520/15) shows poorly circumscribed mass with ill-defined border. Tumor involves surrounding tendon sheath diffusely and focally infiltrates dermis (*arrow*).
B, Axial contrast-enhanced T1-weighted MR image (520/15) shows mass involving ulnar nerve (*arrow*) and tendon sheath of flexor carpi ulnaris (*arrowhead*).
C, Photograph of histopathologic specimen reveals that numerous small nodules consisting of tumor cells infiltrate along ulnar nerve (*arrows*).

In all of our patients, excisional biopsy for definitive diagnosis and primary therapy was performed. However, tumor margins in one of our patients were inadequate and the patient underwent subsequent wide resection. Tumors are often removed piecemeal by surgical procedures, with curative wide resection considered to be the adequate treatment of choice [1].

Grossly, myxoinflammatory fibroblastic sarcoma forms a poorly circumscribed mass surrounding the tendon sheath that may extend into the dermis and skeletal muscle. Microscopically, the tumor is characterized by solid nests of atypical spindle and epithelioid cells in a myxoid stroma and dense inflammatory infiltrates. The tumor cells often have large vesicular nuclei similar to those of virocytes or Reed-Sternberg cells. The immunophenotype is positive for vimentin, with variable immunoreactivity for CD34, CD68, cytokeratin, and smooth-muscle actin [1–6].

On MR images, myxoinflammatory fibroblastic sarcoma typically manifests as a poorly circumscribed mass with a multinodular appearance. Extensive involvement surrounding the tendon sheath is also a common feature.

The appearance of the extension along the tendon sheath in this tumor is similar to that seen in tenosynovitis. Differentiating tenosynovitis from myxoinflammatory fibroblastic sarcoma solely on MRI findings is difficult. Tenosynovitis also can lead to an ill-defined soft-tissue mass or enlargement of its sheath. However, this condition typically manifests as the accumulation of fluid with increased signal intensity of the affected tendon on T2-weighted MR images [8]. Clinical characteristics can allow the differentiation of tenosynovitis from myxoinflammatory fibroblastic sarcoma because tenosynovitis often decreases in size during the course of disease, whereas myxoinflammatory fibroblastic sarcoma usually grows with infiltration [1].

MRI findings of myxoinflammatory fibroblastic sarcoma also closely resemble those of giant cell tumors of the tendon sheath, proliferative fasciitis, acral fibromyxoma, myxoid

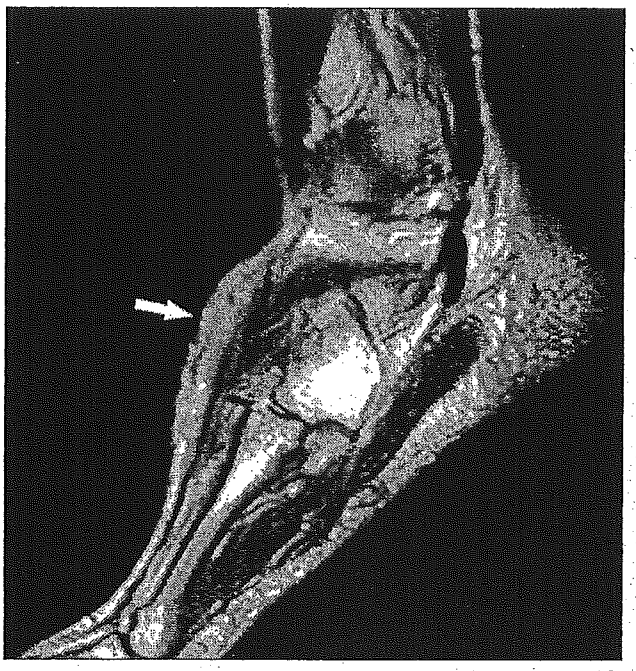

A

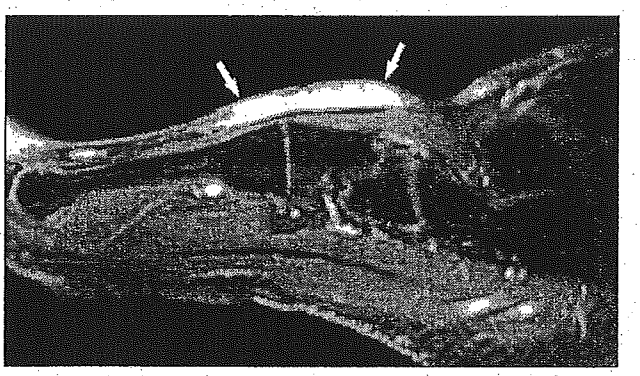

B

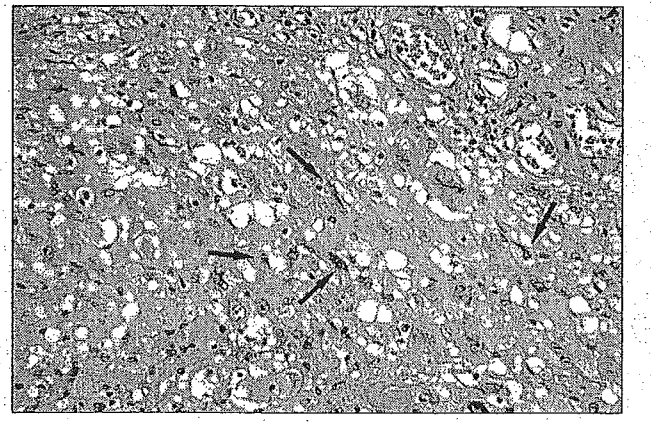

C

Fig. 3.—Myxoinflammatory fibroblastic sarcoma in foot of 32-year-old woman with local recurrence.
A, Sagittal T2-weighted MR image (TR/TE, 3,600/120) shows mass of sheetlike appearance beneath dorsal portion of tendon sheath. Tumor shows intermediate signal intensity, greater than that of muscle (*arrow*).
B, Sagittal contrast-enhanced fat-saturated T1-weighted MR image (520/15) shows homogeneous enhancement of tumor (*arrows*).
C, Photograph of histopathologic specimen shows sheetlike proliferation of spindle-shaped tumor cells (*arrows*) with ganglionlike cells, Reed-Sternberg-like cells, and lymphoid cells surrounding tendon sheaths.

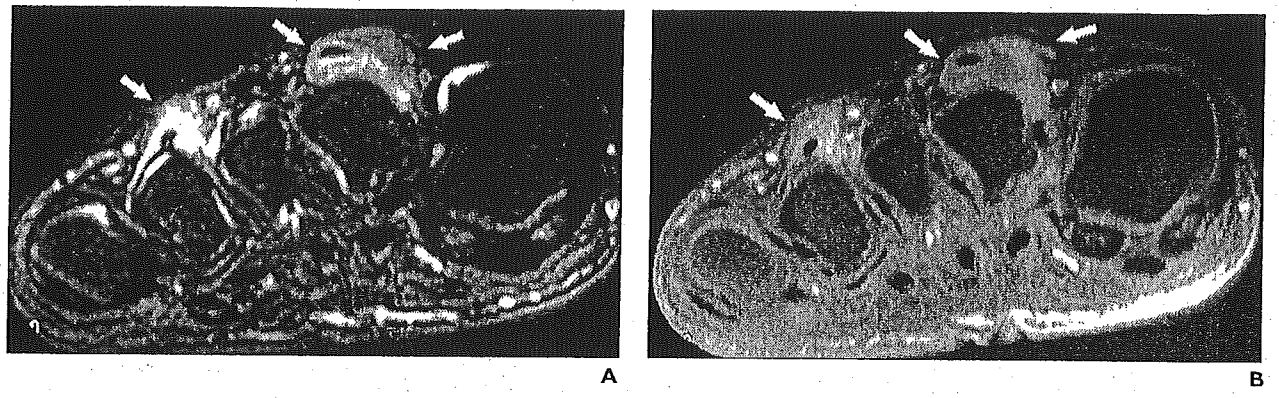

A

B

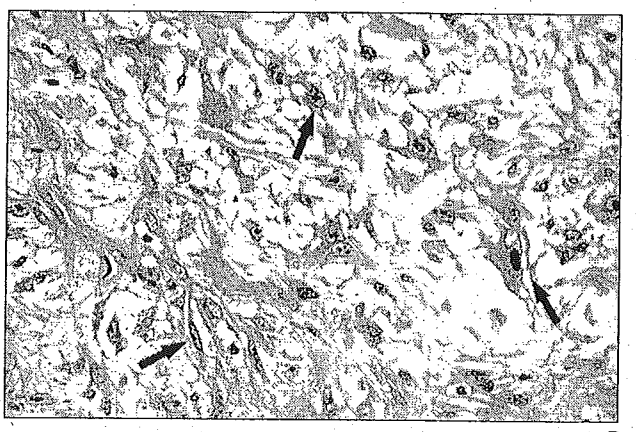

C

Fig. 4.—Myxoinflammatory fibroblastic sarcoma in foot of 24-year-old man with local recurrence.
A, Coronal fat-saturated T2-weighted MR image (TR/TE, 3,500/105) shows mass of branching pattern that occurred along extensor digitorum longus tendon sheaths of second and fourth toes (*arrows*). Tumor shows intermediate signal intensity, greater than that of muscle.
B, Coronal contrast-enhanced T1-weighted MR image (520/15) shows heterogeneous enhancement of tumor (*arrows*).
C, Photograph of histopathologic specimens shows proliferation of spindle-shaped tumor cells (*arrows*) with prominent nucleoli in abundant myxoid stromal matrix.

liposarcoma, and myxofibrosarcoma [9–13]. These conditions could not be distinguished radiologically from myxoinflammatory fibroblastic sarcoma on the basis of our study results. Signal characteristics and enhancement patterns were nonspecific. However, heterogeneous enhancement on contrast-enhanced MR images corresponded to geographic areas of the myxoid stromal matrix in the pathologic specimens. In two of our patients, MRI findings of recurrent tumors were ill defined and the tumors had sheetlike appearances involving the tendon sheath. A significant association may exist between recurrent tumors and the tendon sheath.

In summary, myxoinflammatory fibroblastic sarcoma typically affects adult subjects as a painless mass of the distal extremities at presentation. Myxoinflammatory fibroblastic sarcoma usually manifests on MR images as a multinodular and poorly circumscribed mass involving the surrounding tendon sheath. Although it is unlikely that such a rare condition could reasonably be diagnosed on the basis of MRI findings alone, the condition should be considered in the differential diagnosis of a soft-tissue mass in the distal extremities of adult patients.

References

1. Meis-Kindblom JM, Kindblom LG. Acral myxoinflammatory fibroblastic sarcoma: a low-grade tumor of the hands and feet. *Am J Surg Pathol* 1998;22:911–924
2. Montgomery EA, Devaney KO, Giordano TJ, Weiss SW. Inflammatory myxohyaline tumor of distal extremities with virocyte or Reed-Sternberg-like cells: a distinctive lesion with features simulating inflammatory conditions, Hodgkin's disease, and various sarcomas. *Mod Pathol* 1998;11:384–391
3. Lambert I, Debiec-Rychter M, Guelinckx P, Hagemeijer A, Sciot R. Acral myxoinflammatory fibroblastic sarcoma with unique clonal chromosomal changes. *Virchows Arch* 2001;438:509–512
4. Jurcic V, Zidar A, Montiel MD, et al. Myxoinflammatory fibroblastic sarcoma: a tumor not restricted to acral sites. *Ann Diagn Pathol* 2002;6:272–280
5. Sakaki M, Hirokawa M, Wakatsuki S, et al. Acral myxoinflammatory fibroblastic sarcoma: a report of five cases and review of the literature. *Virchows Arch* 2003;442:25–30
6. Pohar-Marinsek Z, Flezar M, Lamovec J. Acral myxoinflammatory fibroblastic sarcoma in FNAB samples: can we distinguish it from other myxoid lesions? *Cytopathology* 2003;14:73–78
7. Weiss SW, Goldblum JR. *Enzinger and Weiss's soft tissue tumors*, 4th ed. St. Louis, MO: Mosby, 2001:1552–1571
8. Mallefert JF, Dardel P, Cherasse A, Mistrih R, Krause D, Tavernier C. Magnetic resonance imaging in the assessment of synovial inflammation of the hindfoot in patients with rheumatoid arthritis and other polyarthritis. *Eur J Radiol* 2003;47:1–5
9. Llauger J, Palmer J, Monill JM, Franquet T, Bague S, Roson N. MR imaging of benign soft-tissue masses of the foot and ankle. *RadioGraphics* 1998;18:1481–1498
10. Kato K, Ehara S, Nishida J, Satoh T. Rapid involution of proliferative fasciitis. *Skeletal Radiol* 2004;33:300–302
11. Fetsch JF, Laskin WB, Miettinen M. Superficial acral fibromyxoma: a clinicopathologic and immunohistochemical analysis of 37 cases of a distinctive soft tissue tumor with a predilection for the fingers and toes. *Hum Pathol* 2001;32:704–714
12. Tateishi U, Hasegawa T, Beppu Y, Kawai A, Satake M, Moriyama N. Prognostic significance of MRI findings in patients with myxoid-round cell liposarcoma. *AJR* 2004;182:725–731
13. Munk PL, Sallomi DF, Janzen DL, et al. Malignant fibrous histiocytoma of soft tissue imaging with emphasis on MRI. *J Comput Assist Tomogr* 1998;22:819–826

CHEST®

THE CARDIOPULMONARY
AND CRITICAL CARE JOURNAL

FOR PULMONOLOGISTS, CARDIOLOGISTS, CARDIOTHORACIC SURGEONS,
CRITICAL CARE PHYSICIANS, AND RELATED SPECIALISTS

Prediction of Lung Adenocarcinoma Without Vessel Invasion: A CT Scan Volumetric Analysis

Ukihide Tateishi, Hajime Uno, Kan Yonemori, Mistuo Satake, Masahiro Takeuchi and Yasuaki Arai

Chest 2005;128;3276-3283
DOI: 10.1378/chest.128.5.3276

Prediction of Lung Adenocarcinoma Without Vessel Invasion*

A CT Scan Volumetric Analysis

Ukihide Tateishi, MD, PhD; Hajime Uno, PhD; Kan Yonemori, MD; Mistuo Satake, MD; Masahiro Takeuchi, ScD, MPH; and Yasuaki Arai, MD, PhD

Study objectives: **Patients with lung adenocarcinoma without vessel invasion have a favorable prognosis after resection and are among the candidates for limited surgery. The purpose of the present study was to predict lung adenocarcinoma without vessel invasion based on a volumetric analysis of the lesion with a CT scan prior to the operation.**

Methods: **CT scan images were obtained in 288 consecutive patients with adenocarcinoma of the lung before surgical resection. Total tumor volume, the volume of the nonsolid component, and the proportion occupied by the nonsolid component were calculated by the perimeter method. The performance of the derived logistic regression model and the volumetric results were evaluated by receiver operating characteristic analysis. The model derived for the prediction of tumors without vessel invasion was assessed by means of the leave-one-out cross-validation technique.**

Results: **The pathologic diagnosis was adenocarcinoma with vessel invasion in 160 cases, and without vessel invasion in 128 cases. The median total tumor volume, the median volume of the nonsolid component, and median proportion occupied by the nonsolid component were 1,123.7 mm^3, 253.4 mm^3, and 58.0%, respectively. With the derivation of the predictive rule, stepwise regression yielded the following five features: the proportion occupied by the nonsolid component; spiculation; pleural indentation; gender; and tumor size. The Az value, a measure of diagnostic power represented as the area under the curve, was 0.957 for prediction of lung adenocarcinoma without vessel invasion. The cross-validation accuracy achieved by applying the rule was 90.3%.**

Conclusions: **The proportion occupied by the nonsolid component based on a CT scan volumetric analysis was a reliable predictor of tumors without vessel invasion in patients with adenocarcinoma of the lung.**

(CHEST 2005; 128:3276–3283)

Key words: CT scan; lung; lung cancer

Abbreviations: CI = confidence interval; OR = odds ratio; ROC = receiver operating characteristic; SPN = solitary pulmonary nodule

Patients with lung adenocarcinoma without vessel invasion clearly have the best outcome after resection, and they are among the candidates for limited surgery.[1,2] Some studies[3,4] have highlighted the potential diagnostic role of thin-section CT scanning in identifying nonsolid components of adenocarcinoma of the lung. The nonsolid component is larger in patients with noninvasive tumors and has been shown to discriminate between patients with noninvasive tumors and patients with advanced tumors with a high degree of power.[5] In addition, the proportion of the tumor occupied by the nonsolid component correlates well with the absence of vascular or lymphatic invasion and with better outcome.[6–10] Thus, identification of the size of the nonsolid component on CT scan images of lung adenocarcinoma is a potential surrogate measurement for tumor aggressiveness.

The reliability of almost all data on the proportion

*From the Division of Diagnostic Radiology (Drs. Tateishi, Yonemori, Satake, and Arai), National Cancer Center Hospital, Tokyo, Japan; the Department of Biostatistics (Dr. Uno), Harvard School of Public Health, Boston, MA; and the Division of Biostatistics (Takeuchi), Kitasato University Graduate School, Tokyo, Japan.

Dr. Uno received support for this research by Banyu Life Science Foundation International.

Manuscript received January 12, 2005; revision accepted May 4, 2005.

Correspondence to: Ukihide Tateishi, MD, PhD, Division of Diagnostic Radiology, National Cancer Center Hospital, Tsukiji, Chuo-Ku, 104-0045, Tokyo, Japan; e-mail: utateish@ncc.go.jp

occupied by the nonsolid component is limited, because the investigators assumed that the lesions were spherical and used the maximum cross-sectional diameter on CT scan images to calculate it,[5,6] and the only large series to date used the maximum cross-sectional area of the tumor to predict invasion.[11] To our knowledge, few studies have used CT scanning to calculate the volume of the nonsolid component within tumors and to correlate the proportion occupied by the nonsolid component with pathologic characteristics of tumor invasion. Moreover, most studies to date have proposed diagnostic criteria for lesions without testing their diagnostic validity.[6–11]

We therefore conducted both a derivation and validation cohort study of patients with adenocarcinoma of the lung in order to predict tumors without vessel invasion. Our results will assist physicians in estimating more accurately the probability of a tumor being unassociated with vessel invasion and to decide whether further investigation is necessary to rule the presence of a noninvasive tumor in or out.

Materials and Methods

A retrospective review of the pathologic records for the period between October 2001 and January 2004 identified 288 who had been patients treated for adenocarcinoma of the lung the maximum dimension of which was < 2 cm. A consecutive subset of 288 patients contributed to the derivation analysis and the cross-validation analysis based on the leave-one-out method. The study population consisted of 113 men and 175 women, and their mean age was 64.7 years (age range, 41 to 86 years). All patients had undergone surgical resection consisting of wedge resection or lobectomy. Complete dissection (n = 96; 33%) and sampling of mediastinal or hilar lymph nodes (n = 192; 67%) were performed. The nodes included high and low ipsilateral, paratracheal, subcarinal, and inferior pulmonary ligament lymph nodes, and any other suspicious lymph nodes identified at surgery. Surgical specimens were fixed in formalin and embedded in paraffin. Four-micrometer sections were stained with hematoxylin and eosin and elastica-van Gieson stain. Tumors without vessel invasion were diagnosed when no lymphatic or blood vessel invasion was identified within the lesion microscopically. Based on the current international TNM classification for staging lung cancer,[12] 274 tumors (95%) were classified as stage Ia, and the other 14 tumors (5%) were classified as stage IIa. The clinical records of all patients were available for review. No patients were lost to follow-up, which began on the date of the initial operation. The median duration of follow-up was 22 months, and ranged from 1 to 40 months. This study was approved by our institutional review board after confirmation of informed consent by the patients to a review of their records and images.

CT scanning was performed with a multidetector scanner (Aquilion V-detector; Toshiba Medical Systems; Tokyo, Japan) by using axial 2.0-mm × 4 or 1.0-mm × 16 modes (*ie*, 4 or 16 images per gantry rotation), 120 kVp, 200 to 250 mA, and a 0.5-s scanning time. Thin-section CT scan images were obtained using 2.0-mm sections that were reconstructed at 2.0-mm intervals by means of a high-spatial frequency algorithm and were retrospectively retargeted to each lung with a 20-cm field of view. All images were displayed at window settings for lung (center, −600 Hounsfield units; width, 2,000 Hounsfield units). Image viewing and manipulation were controlled with a workstation (ZIOSOFT M900, Quadra, version 3.10f; ZIOSoft Inc; Tokyo, Japan) that allows the reader to draw lines through regions of interest and the perimeters around them.

The CT scan images were assessed in random order by two independent observers without reference to the clinical findings. The observers examined the images for the following: maximum tumor diameter; nodular edge (irregular or not); presence of a nonsolid component; presence of an air-bronchogram; presence of cavitation, lobulation, pleural indentation, bubble-like lucencies, spiculation, vascular convergence, bronchiectasis, or bronchiolectasis; and the lobe in which the lesion was located (*eg*, upper, middle, or lower). *Nonsolid component* was defined as an area of ground-glass attenuation or hazy increased parenchymal attenuation without obscuring of the underlying vascular markings. We distinguished between *nonsolid tumors* and *part-solid tumors*, with the former being defined as tumors containing only a nonsolid component, and the latter as tumors that contained a partially solid component. Bubble-like lucencies were diagnosed when there were multiple cystic air spaces measuring ≤ 5 mm in diameter within the lesion surrounded by a wall of variable thickness.[13] After an initial independent evaluation, the two observers reviewed all cases in which their interpretations disagreed and reached a final decision by consensus.

The volume of each tumor was calculated by the perimeter method.[14–16] The cross-sectional areas of the entire tumor and of the solid component were calculated by a workstation that manipulates a voxel matrix of 512 × 512 pixels. Two board-certified radiologists who were experienced with image-viewing and image-manipulation software drew a line around the perimeter of each tumor twice. The total tumor volume and the volume of the solid component were calculated by summing the cross-sectional areas and multiplying by the section increment. The volume of the nonsolid component was calculated by subtracting the volume of the solid component from the total volume. The averages of the two volume values calculated by each of the two observers were used in the analyses.

Statistical Analysis

Interobserver variation in relation to CT scan findings was quantified as the weighted κ coefficient of agreement. The predictive performance of volumetric data was evaluated by receiver operating characteristic (ROC) analysis, and the areas under curve were represented by the Az values, which are a measure of diagnostic power represented by the area under the curve.[17,18] A stepwise procedure was used in the logistic regression analysis to select the independent variables that should have been included in the model to predict tumors without vessel invasion. A variable was entered into the model if the probability of its score statistic was < 0.05. The odds ratio (OR) and 95% confidence interval (CI) for the multivariate predictors were estimated. The Hosmer-Lemeshow test was also performed to evaluate goodness-of-fit.[19] Calibration curves comparing the observed proportion of tumors without vessel invasion with the probability of tumors without vessel invasion ordered by the increasing probability of tumors without vessel invasion were constructed. The performance of the learned model was verified by using the leave-one-out cross-validation method, in which all cases but one were used to train the prediction rule, which was then applied to the single excluded case.[20–22] This procedure was repeated for each case, until each case had been left out only once. Cross-validation accuracy was calculated by comparing the predicted response and the observed response.[23] The following variables were considered for their prognostic value: age; gender;

Table 1—*Patient Demographics

Characteristics	No Vessel Invasion (n = 128)	Vessel Invasion (n = 160)
Gender		
Male	39 (30)	74 (46)
Female	89 (70)	86 (54)
Age,† yr		
Mean	64	65.4
SD	9.1	8.8
Range	41–84	41–86
Location of tumor		
Upper lobe	78 (61)	91 (57)
Middle lobe	14 (11)	5 (3)
Lower lobe	36 (28)	64 (40)
Tumor size,† mm		
Mean	12.4	15.8
SD	4.5	3.5
Range	5.0–20.0	7.0–20.0
Tumor with nonsolid component	124 (97)	78 (49)
Nonsolid tumor	81 (63)	1 (1)
Part-solid tumor	43 (34)	77 (48)
Solid tumor	4 (3)	82 (51)

*Values are given as No. (%).

†The differences between two groups were assessed by a two-sample *t* test. The two tumor subgroups differed significantly in terms of gender (p 0.01 [χ^2 test]). Tumors without vessel invasion were significantly more frequent (p 0.01 [χ^2 test]) in the upper lobe than those with vessel invasion. Tumor size was significantly smaller in tumors without vessel invasion (p 0.01 [*t* test]) than that in tumors with vessel invasion. Tumors with a nonsolid component were significantly more frequent (p 0.0001 [χ^2 test]) among tumors without vessel invasion.

presence or absence of vessel invasion; tumor size; total tumor volume; the volume of the nonsolid component; the proportion occupied by the nonsolid component; and CT scan findings. Univariate analysis was performed by comparing Kaplan-Meier disease-free or recurrence-free survival curves and carrying out log-rank tests. All analyses were conducted using a statistical software package (SAS, version 8.2; SAS Institute, Cary, NC; and R software, version 1.9.0; R project, Center for Computational Intelligence; Vienna, Austria).

Results

The clinical characteristics and outcomes of all patients with adenocarcinoma of the lung are summarized in Table 1. The pathologic diagnosis was lung adenocarcinoma with vessel invasion in 160 of the 288 patients (55.6%), and without vessel invasion in the other 128 patients (44.4%). Female patients had a predilection for tumors without vessel invasion according to the results of the univariate analysis. The median age at presentation was 66 years (age range, 41 to 86 years). Age was not statistically associated with tumor type. Most tumors (n = 169; 58.7%) were in the upper lobe. The median tumor size was 15.0 mm (range, 5.0 to 20.0 mm). Tumors with vessel invasion were significantly larger than tumors without vessel invasion. Among the tumors without vessel invasion, nonsolid tumors (n = 81; 28.1%) were more common than part-solid or solid tumors (n = 47; 16.3%); whereas, among the tumors with vessel invasion, solid or part-solid tumors (n = 159; 55.2%) were more common than nonsolid tumors (n = 1; 0.3%). Tumors with a nonsolid component were more common among the tumors without vessel invasion than among the tumors with vessel invasion.

There was good interobserver agreement in the analysis of the CT scan findings (weighted κ coefficient, 0.63 to 0.79). The following CT scan findings were more frequently identified in tumors with vessel invasion than in tumors without vessel invasion according to the univariate analysis: cavitation; air bronchogram;

Table 2—*Summary Statistics of Volumetric Measurements

Variables	No Vessel Invasion	Vessel Invasion
Tumor volume, mm^3		
Mean	1,155.7	1,773.6
SD	1,411.1	1,321.3
Q1-Median-Q3	247.6–713.8–1,544.6	867.1–1,492.5–2,367.4
Range	43.6–6,828.0	120.8–6,912.2
Volume of nonsolid component, mm^3		
Mean	1,027.5	496.9
SD	1,372.7	829.6
Q1-Median-Q3	157.5–567.7–1,413.3	0.0–0.0–658.5
Range	0.0–6,593.4	0.0–4583.6
Proportion of nonsolid component, %		
Mean	88.1	24.3
SD	26.4	33.2
Q1-Median-Q3	93.4–100.0–100.0	0.0–0.0–41.4
Range	0.0–100.0	0.0–100.0

*The differences between two groups were assessed by the Wilcoxon two-sample *t* test. The tumor subgroups differed significantly in terms of the volume of those three kinds of measurements (p 0.0001). Q1 = 25th percentile; Q3 = 75th percentile.

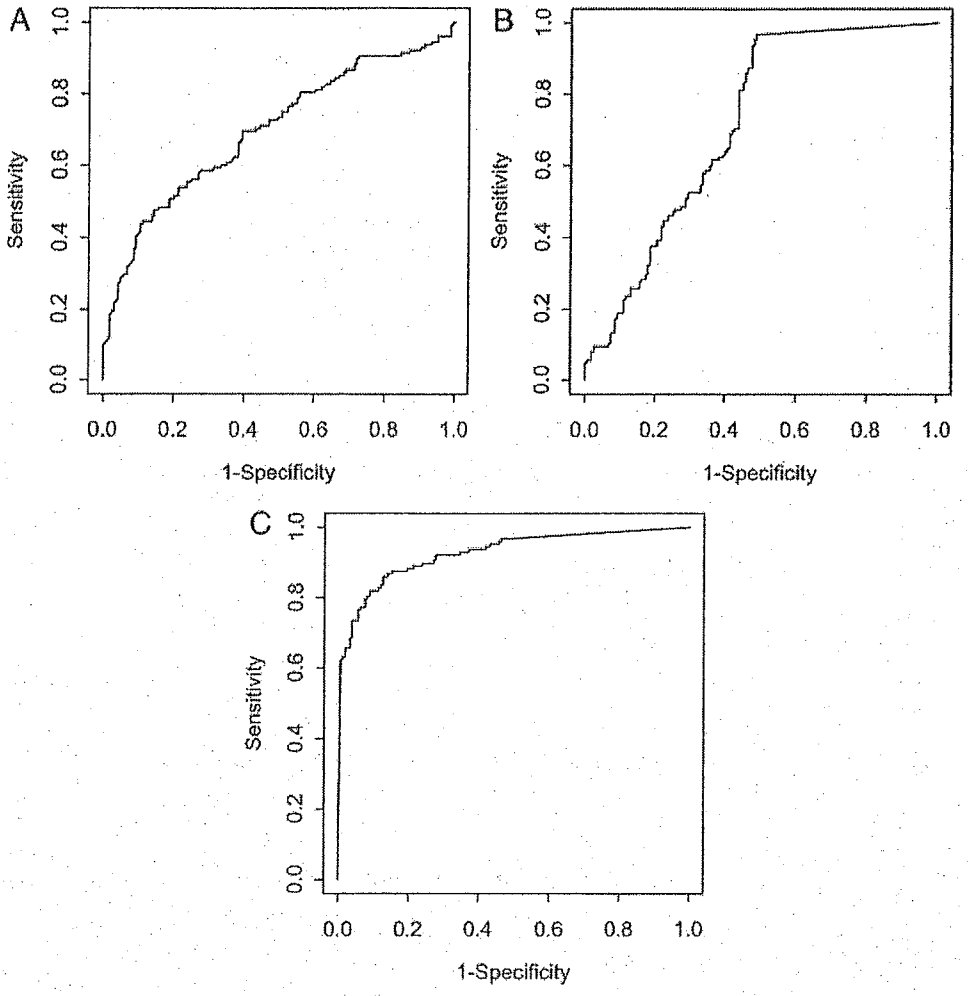

FIGURE 1. *Top, A*: ROC curve for total tumor volume determined by the perimeter method. The mean (± SE) Az value was 0.699 ± 0.030. *Middle, B*: the ROC curve for the volume of the nonsolid component determined by the perimeter method. The mean Az (± SE) value was 0.714 ± 0.030. *Bottom, C*: ROC curve for the proportion occupied by the nonsolid component determined by the perimeter method. The mean Az (± SE) value was 0.928 ± 0.015.

irregular margin; speculation; lobulation; and bronchiectasis or bronchiolectasis. Irregular margins were common in tumors without vessel invasion but were more frequent in tumors with vessel invasion. Vascular convergence was a less common finding and was noted only in patients with tumors that were associated with vessel invasion. Bubble-like lucencies were observed in one tumor with vessel invasion and in one tumor without vessel invasion.

Volumetric Analysis

The results of the volumetric analysis are summarized in Table 2. The median total tumor volume, the median volume of the nonsolid component, and the median proportion occupied by the nonsolid component were 1,123.7 mm^3 (range, 43.6 to 6,912.2 mm^3), 253.4 mm^3 (range, 0 to 6,593.4 mm^3), and 58.0% (range, 0 to 100%), respectively. Significant differences were found between the mean values for total volume and the proportion values in two groups. The ROC analyses to predict tumors without vessel invasion revealed that Az values of total tumor volume, the volume of the nonsolid component, and the proportion occupied by the nonsolid component were 0.699 (95% CI, 0.638 to 0.760), 0.714 (95% CI, 0.653 to 0.775), and 0.928 (95% CI, 0.895 to 0.961), respectively (Fig 1). The potential predictors of tumors without vessel invasion at the threshold of each median value were as follows: total tumor volume; the volume of the nonsolid component; and the proportion occupied by the nonsolid component (Table 3). Univariate analysis showed that our pre-

Table 3—*Potential Predictors of Tumors Without Vessel Invasion

Criteria	Proportion of Tumors Without Vessel Invasion, %	OR	95% CI	p Value†
Gender		1.9636	1.2053–3.1992	0.0064
Female	50.9			
Male	34.5			
Age		1.1124	0.6983–1.7723	0.6543
≤ 66 yr	45.7			
> 66 yr	43.1			
Tumor size		4.0588	2.4416–6.7472	< 0.0001
≤ 15 mm	58.5			
> 15 mm	25.8			
Air bronchogram		0.1143	0.0585–0.2235	< 0.0001
Positive	13.6			
Negative	58.0			
Irregular margin		0.1605	0.0636–0.4049	< 0.0001
Positive	40.1			
Negative	80.6			
Spiculation		0.0349	0.0159–0.0767	< 0.0001
Positive	7.1			
Negative	68.6			
Lobulation		0.1496	0.0185–1.2122	0.0412
Positive	11.1			
Negative	45.5			
Pleural indentation		0.1148	0.0673–0.1961	< 0.0001
Positive	21.2			
Negative	70.1			
Bubble-like lucencies		1.2540	0.1742–9.0269	0.8221
Positive	50.0			
Negative	44.4			
Vascular convergence		NA	NA	< 0.0001
Positive	0.0			
Negative	50.0			
Bronchiectasis or bronchiolectasis		0.2150	0.0468–0.9882	0.0312
Positive	15.4			
Negative	45			
Tumor volume		2.9934	1.8465–4.8528	< 0.0001
≤ 1,123.7 mm^3	57.6			
> 1,123.7 mm^3	31.3			
Volume of nonsolid component		2.6535	1.6431–4.2853	< 0.0001
> 253.4 mm^3	56.3			
≤ 253.4 mm^3	32.6			
Proportion of nonsolid component		42.778	21.5856–84.7761	< 0.0001
> 80%	84.6			
≤ 80%	11.4			

*The median value was considered to be a cutoff in age, tumor size, tumor volume, the volume of the nonsolid component, and the proportion of the nonsolid component. NA = not applicable.
†χ^2 test.

dictor of interest, the proportion occupied by the nonsolid component, was highly predictive of tumors without vessel invasion at an OR of 42.8 (95% CI, 21.6 to 84.8) with 80.0% as the threshold value.

Derivation of the Prediction Rule

From the 13 variables that reached the level of statistical significance in the univariate analyses comparing tumors with and without vessel invasion, we excluded location of the tumor because the absolute difference fell within the precision range of the test. The logistic regression analysis identified the following five significant predictors of tumors without vessel invasion: proportion occupied by the nonsolid component; spiculation; pleural indentation; gender; and tumor size (Table 4). The Az value of the ROC analysis for prediction of a tumor without vessel invasion in the derivation phase was 0.957 (Fig 2). We adopted the threshold that yielded an appropriate tradeoff between sensitivity and specificity (*ie*, probability of a tumor without vessel invasion, 0.5). At that point in the ROC curve, the sensitivity, specificity, accuracy, positive predictive value, and

Table 4—*Significant Predictors of Tumors Without Vessel Invasion*

Variables	Coefficient	OR*	95% CI	p Value
Intercept	−1.6729			
Proportion of nonsolid component > 80% vs ≤ 80%	3.5744	35.673	14.392–88.421	< 0.0001
Positive vs negative spiculation	−2.3889	0.092	0.032–0.261	< 0.0001
Positive vs negative pleural indentation	−1.3982	0.247	0.101–0.602	0.0021
Female vs male gender	1.0056	2.734	1.141–6.551	0.0241
Tumor size ≤ 15 mm vs > 15.0 mm	1.1271	3.087	1.249–7.627	0.0146

*OR was presented to predict tumors without vessel invasion.

negative predictive value of the rule were 88.3%, 91.9%, 90.3%, 89.7%, and 90.7%, respectively. The results of the goodness-of-fit test (χ^2, 3.6563; degrees of freedom, 8; $p = 0.89$) indicated that the observed proportion of patients with tumors without vessel invasion was similar to the predicted proportion in the derivation group. The calibration curves for the derivation data demonstrated good calibration of the prediction rule.

Cross-Validation Accuracy

When the rule derived from the 288 patients was applied to the leave-one-out cross-validation cohort, the validation accuracy based on the leave-one-out method was 90.3%, which was quite similar to the model accuracy, suggesting that the rule that was derived to predict tumors without vessel invasion is stable.

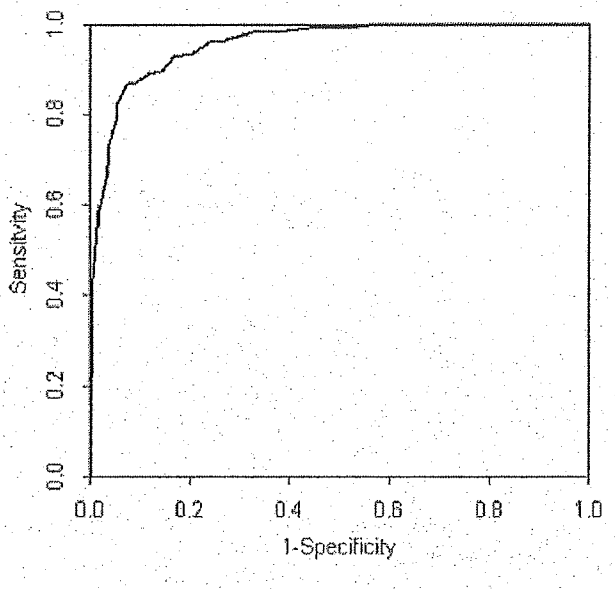

FIGURE 2. ROC curve for the derived model to predict tumor without vessel invasion. The probability of the occurrence of a tumor without vessel invasion based on the derived model can be considered diagnostic, and the tradeoff between sensitivity and specificity at various thresholds of the probability of a tumor without vessel invasion is given by the ROC curve.

Prognostic Analysis

At the last follow-up, 1 of the 288 patients (0.3%) had died, 12 patients (4.2%) were alive with recurrent disease, and the 5-year overall survival rate was 98.7%. Univariate analysis revealed that none of the variables had a significant impact on overall survival. The 5-year recurrence-free survival rate was 83.5%. The patients with tumors without vessel involvement had a 5-year recurrence-free rate of 88.0%, which was significantly better than the rate of 74.6% among the patients with vessel invasion ($p < 0.05$). Cavitation and vascular convergence were significantly associated with recurrence-free survival according to the univariate analysis ($p < 0.01$).

DISCUSSION

The proportion occupied by the nonsolid component is characteristically higher in patients with lung adenocarcinoma without vessel invasion, and several studies[4,5] have demonstrated that it distinguishes tumors without vessel invasion from tumors with vessel invasion. Nevertheless, controversy remains regarding its reproducibility in optimally distinguishing tumors without vessel invasion from tumors with vessel invasion. In this study, we investigated the diagnostic capacity of the proportion occupied by the nonsolid component to predict tumors without vessel invasion in a well-characterized study population.

We performed ROC analysis to assess the ability of the proportion occupied by the nonsolid component to discriminate between tumors with and without vessel invasion. We have documented that the diagnostic probability of the proportion occupied by the nonsolid component for tumors without vessel invasion is accurate. The Az value observed for the proportion occupied by the nonsolid component was 0.957. In our study population, its discriminatory capacity yielded positive and negative predictive values for tumors without vessel invasion of 89.7% and 90.7%, respectively. These observations suggest that the identification of the proportion occupied by the nonsolid component on CT images may be useful

for predicting tumors without vessel invasion in patients with adenocarcinoma of the lung.

At both baseline screenings and repeat CT screenings for lung cancer, tumors containing a nonsolid component have been found to be a significant sign of malignancy.[24] Henschke and colleagues[25] found that 19% of the 233 cases with positive results at baseline screening had a tumor with the nonsolid component and that the tumors were predominantly bronchioloalveolar carcinoma and adenocarcinoma with bronchioloalveolar carcinoma features. These predominant histologic types of malignancy corresponded to noninvasive and invasive tumors of lung adenocarcinoma. The quantification of the extent or growth rate of the solid and nonsolid components of tumors is necessary during CT scan screening for lung cancer.

Swensen and colleagues[18] created a multivariate logistic regression model to predict a malignant solitary pulmonary nodule (SPN) in a derivation and validation analysis. Of 629 radiologically intermediate nodules in their study, 23% were malignant SPNs. The investigators identified the following three independent findings that predicted malignant SPNs: upper lobe distribution; tumor size; and spiculation. Among these findings, spiculation was associated with the prediction model in our results. Pleural indentation and male predilection were also significant predictors of tumors with vessel invasion in our study.

Some studies[26–28] using the segmentation algorithm of software have yielded calculations of tumor volume in three dimensions. The excellent interobserver variability suggests that tumor volume estimations by different observers can be reliably compared when three-dimensional volumetric software is used. However, this technique does not enable the segmentation of tumors that contain a nonsolid component.[27,28] Since most tumors in our study contained a nonsolid component and were not appropriate for three-dimensional volumetric analysis, tumor volume was calculated by the perimeter method, which had potential sources of error that affected the results of volumetric analyses.[29]

The proportion occupied by the nonsolid component was dichotomized using the median value for a threshold level in the univariate and multivariate analyses performed. In both the univariate and multivariate analyses, the proportion occupied by the nonsolid component yielded the highest point estimates and CIs for the ORs of tumors without vessel invasion. However, it should be noted that there was enough of a difference between the values for patients in whom the nonsolid component occupied a high proportion of the tumor and those for patients in whom the nonsolid component occupied a small proportion of the tumor that similar results could have been obtained with different threshold values.

There are other potential limitations of this study. The size of the sample may also have led to false-positive results because of the number of covariates included in the initial analysis. However, the strength of the association with our primary outcome of interest, as well as the historical precedence of other significant predictors in our multivariate analysis, lends credence to our conclusions. In summary, the results of our study confirm that the proportion occupied by the nonsolid component of a tumor on CT scans is a reliable predictor of tumors without vessel invasion with much greater confidence than was possible in the past.

References

1 Travis WD, Colby TV, Corrin B, et al. Histological typing of lung and pleural tumors. Berlin, Germany: Springer, 1999

2 Noguchi M, Morikawa A, Kawasaki M, et al. Small adenocarcinoma of the lung: histologic characteristics and prognosis. Cancer 1995; 75:2844–2852

3 Jang HJ, Lee KS, Kwon OJ, et al. Bronchioloalveolar carcinoma: focal area of ground-glass attenuation at thin-section CT as an early sign. Radiology 1996; 199:485–488

4 Kuriyama K, Seto M, Kasugai T, et al. Ground-glass opacity on thin-section CT: value in differentiating subtypes of adenocarcinoma of the lung. AJR Am J Roentgenol 1999; 173:465–469

5 Ohde Y, Nagai K, Yoshida J, et al. The proportion of consolidation to ground-glass opacity on high resolution CT is a good predictor for distinguishing the population of non-invasive peripheral adenocarcinoma. Lung Cancer 2003; 42: 303–310

6 Aoki T, Tomoda Y, Watanabe H, et al. Peripheral lung adenocarcinoma: correlation of thin-section CT findings with histologic prognostic factors and survival. Radiology 2001; 220:803–809

7 Suzuki K, Yokose T, Yoshida J, et al. Prognostic significance of the size of central fibrosis in peripheral adenocarcinoma of the lung. Ann Thorac Surg 2000; 69:893–897

8 Kodama K, Higashiyama M, Yokouchi H, et al. Prognostic value of ground-glass opacity found in small lung adenocarcinoma on high-resolution CT scanning. Lung Cancer 2002; 33:17–25

9 Matsunaga H, Yokoi K, Anraku M, et al. Proportion of ground-glass opacity on high-resolution computed tomography in clinical T1N0M0 adenocarcinoma of the lung: a predictor of lymph node metastasis. J Thorac Cardiovasc Surg 2002; 124:278–284

10 Kim EA, Johkoh T, Lee KS, et al. Quantification of ground-glass opacity on high-resolution CT of small peripheral adenocarcinoma of the lung: pathologic and prognostic implications. AJR Am J Roentgenol 2001; 177:1417–1422

11 Takashima S, Maruyama Y, Hasegawa M, et al. Prognostic significance of high-resolution CT findings in small peripheral adenocarcinoma of the lung: a retrospective study on 64 patients. Lung Cancer 2002; 36:289–295

12 Lababede O, Meziane MA, Rice TW. TNM staging of lung cancer: a quick reference chart. Chest 1999; 115:233–235

13 Adler B, Padley S, Miller RR, et al. High-resolution CT of bronchioloalveolar carcinoma. AJR Am J Roentgenol 1992; 159:275–277

14 Winter-Muram HT, Jennings SG, Tarver RD, et al. Volumetric growth rate of stage I lung cancer prior to treatment: serial CT scanning. Radiology 2002; 223:798–805
15 Winter-Muram HT, Jennings SG, Meyer CA, et al. Effect of varying CT section width on volumetric measurement of lung tumors and application of compensatory equations. Radiology 2003; 229:184–194
16 Jennings SG, Winter-Muram HT, Tarver RD, et al. Lung tumor growth: assessment with CT-comparison of diameter and cross-sectional area with volume measurements. Radiology 2004; 231:866–871
17 Hanley JA, McNeil BJ. The meaning and use of the area under a receiver operating characteristic (ROC) curve. Radiology 1982; 143:29–36
18 Swensen SJ, Silverstein MD, Ilstrup DM, et al. The probability of malignancy in solitary pulmonary nodules: application to small radiologically intermediate nodules. Arch Intern Med 1997; 157:849–855
19 Lemeshow S, Hosmer DW. A review of goodness-of-fit statistics for use in the development of logistic regression models. Am J Epidemiol 1982; 115:92–106
20 Wasson JH, Sox HC, Neff RK, et al. Clinical prediction rules: applications and methodological standards. N Engl J Med 1985; 313:793–799
21 Scott JA. Pulmonary perfusion patterns and pulmonary arterial pressure. Radiology 2002; 224:513–518
22 Arana E, Delicado P, Marti-Bonmati L. Validation procedures in radiologic diagnostic models: neural network and logistic regression. Invest Radiol 1999; 34:636–642
23 Stone M. Cross-validatory choice and assessment of statistical predictions. J R Stat Soc B 1974; 36:111–147
24 Henschke CI, McCauley DI, Yankelevitz DF, et al. Early lung cancer action project: overall design and findings from baseline screening. Lancet 1999; 354:99–105
25 Henschke CI, Yankelevitz DF, Mircheva R, et al. CT screening for lung cancer: frequency and significance of part-solid and nonsolid nodules. AJR Am J Roentgenol 2002; 1178: 1053–1057
26 Yankelevitz DF, Reeves AP, Kostis WJ, et al. Small pulmonary nodules: volumetrically determined growth rates based on CT evaluation. Radiology 2000; 217:251–256
27 Revel MP, Lefort C, Bissery A, et al. Pulmonary nodules: preliminary experience with three-dimensional evaluation. Radiology 2004; 231:459–466
28 Revel MP, Bissery A, Bienvenu M, et al. Are two-dimensional CT measurements of small noncalcified pulmonary nodules reliable? Radiology 2004; 231:453–458
29 Staron RB, Ford E. Computed tomographic volumetric calcification reproducibility. Invest Radiol 1986; 21:272–274

Prediction of Lung Adenocarcinoma Without Vessel Invasion: A CT Scan Volumetric Analysis

Ukihide Tateishi, Hajime Uno, Kan Yonemori, Mistuo Satake, Masahiro Takeuchi and Yasuaki Arai

Chest 2005;128;3276-3283
DOI: 10.1378/chest.128.5.3276

Jpn J Clin Oncol 2005;35(8)444–452
doi:10.1093/jjco/hyi128

Incidence of Multiple Primary Malignancies in a Cohort of Adult Patients with Soft Tissue Sarcoma

Ukihide Tateishi[1], Tadashi Hasegawa[2], Seiichiro Yamamoto[3], Umio Yamaguchi[4], Ryohei Yokoyama[5], Hiroshi Kawamoto[3], Mitsuo Satake[1] and Yasuaki Arai[1]

[1]Diagnostic Radiology Division, [2]Pathology Division and [4]Orthopedic Surgery Division, National Cancer Center Hospital and Institute, [3]Statistics and Cancer Control Division, Research Center for Cancer Prevention and Screening, National Cancer Center, Tokyo and [5]Department of Orthopedic Surgery, Kyushu Cancer Center, Fukuoka, Japan

Received March 6, 2005; accepted June 1, 2005; published online July 15, 2005

Objective: Some studies to date have suggested the development of multiple primary malignancies in patients with soft tissue sarcoma. The current study was performed to quantify the risk of development of multiple primary malignancies in adult patients with soft tissue sarcoma.
Methods: A total of 406 consecutive patients who were diagnosed with soft tissue sarcoma were identified in the study analysis. The cumulative incidence of multiple malignancies was calculated by comparing Kaplan–Meier curves and log-rank tests from each histological type. A Cox proportional hazards model was used to estimate the influence on the hazard ratio (HR) of each variable.
Results: A total of 35 patients with soft tissue sarcoma (9%), having preceding ($n = 15$) and subsequent ($n = 20$) malignancies other than soft tissue sarcoma were documented. The 5- and 10-year estimated cumulative incidence of multiple primary malignancies were 7.6 and 12.3%, respectively. The hazard risk of multiple primary malignancies adjusted for potential confounding variables was significantly associated with age at diagnosis (HR = 1.51, $P = 0.0019$). The risk of multiple primary malignancies was also increased in patients with myxofibrosarcoma adjusted by the potential confounding variables (HR = 2.34, $P = 0.048$). The 5- and 10-year estimated cumulative incidence of multiple primary malignancies in patients with myxofibrosarcoma were both 16.9%.
Conclusion: The results of our study confirm that the risk of multiple malignancies appears to be impacted by age at the time of diagnosis of the first tumor and by the histological type of myxofibrosarcoma.

Key words: soft tissue sarcoma – myxofibrosarcoma – multiple malignancies – second primary tumor

INTRODUCTION

The development of multiple malignancies in a single individual has been reported after successful treatment of primary tumors (1,2). The greatest attention has been focused on second primary tumors (SPTs) after treatment of malignant lymphoma (3), retinoblastoma (4) and malignant germ cell tumor (5,6) because good cure rates have been achieved for many years, resulting in many long-term survivors.

The occurrence of multiple malignancies in patients with soft tissue sarcoma (STS) has also been reported (7,8). Studies focused on patients with osteosarcoma have revealed an overall 10-year cumulative incidence of SPT of 2.0–3.1% (9,10). Adult patients with STS have been found to develop other malignant neoplasms either before or after the diagnosis of STS, and this phenomenon occurred at a significantly higher rate than reported for the occurrence of STS in the general cancer population (11).

However, the risk of SPT after treatment of the first tumor has been mainly described in children with STS. Although we have observed the occurrence of multiple primary malignancies that occurred in adult patients with various histological types of STS, especially pleomorphic malignant fibrous histiocytoma (MFH) and myxofibrosarcoma, in daily clinical practice there has been little information on the management of these patients. The current study was therefore undertaken to assess the risk of development of another primary malignant tumor in adult patients with STS.

MATERIALS AND METHODS

PATIENTS

The records of 500 consecutive adult STS patients diagnosed and treated between February 1962 and August 2003 were

For reprints and all correspondence: Ukihide Tateishi, Division of Diagnostic Radiology, National Cancer Center Hospital, 5-1-1, Tsukiji, Chuo-ku, 104-0045 Tokyo, Japan. E-mail: utateish@ncc.go.jp